



**HAL**  
open science

# Determination of elastic strain fields and geometrically necessary dislocation distributions near nanoindentations using electron back scatter diffraction

Angus Wilkinson, David Randman

► **To cite this version:**

Angus Wilkinson, David Randman. Determination of elastic strain fields and geometrically necessary dislocation distributions near nanoindentations using electron back scatter diffraction. *Philosophical Magazine*, 2010, 90 (09), pp.1159-1177. 10.1080/14786430903304145 . hal-00581027

**HAL Id: hal-00581027**

**<https://hal.science/hal-00581027>**

Submitted on 30 Mar 2011

**HAL** is a multi-disciplinary open access archive for the deposit and dissemination of scientific research documents, whether they are published or not. The documents may come from teaching and research institutions in France or abroad, or from public or private research centers.

L'archive ouverte pluridisciplinaire **HAL**, est destinée au dépôt et à la diffusion de documents scientifiques de niveau recherche, publiés ou non, émanant des établissements d'enseignement et de recherche français ou étrangers, des laboratoires publics ou privés.



**Determination of elastic strain fields and geometrically necessary dislocation distributions near nanoindents using electron back scatter diffraction**

Journal:	<i>Philosophical Magazine &amp; Philosophical Magazine Letters</i>
Manuscript ID:	TPHM-09-May-0185.R1
Journal Selection:	Philosophical Magazine
Date Submitted by the Author:	10-Aug-2009
Complete List of Authors:	Wilkinson, Angus; University of Oxford, Department of Materials Randman, David; University of Sheffield, Department of Engineering Materials
Keywords:	dislocation mechanics, dislocations, electron diffraction, electron microscopy, mechanics of materials, nanoindentation
Keywords (user supplied):	EBSD



# Determination of elastic strain fields and geometrically necessary dislocation distributions near nanoindents using electron back scatter diffraction

Angus J Wilkinson<sup>1</sup> & David Randman<sup>2</sup>

Department of Materials, University of Oxford, Parks Road, Oxford OX1 3PH, U.K.

<sup>1</sup> angus.wilkinson@materials.ox.ac.uk

<sup>2</sup> d.randman@sheffield.ac.uk, (now at IMPPETUS, Department of Engineering Materials, University of Sheffield, Sheffield S1 3JD, U.K.)

## Abstract

The deformation around a 500 nm deep Berkovich indent in a large grained Fe sample has been studied using high resolution electron back scatter diffraction (EBSD). EBSD patterns were obtained in a two dimensional map around the indent on the free surface. A cross correlation based analysis of small shifts in many sub-regions of the EBSD patterns was used to determine the variation of elastic strain and lattice rotations across the map at a sensitivity of  $\sim\pm 10^{-4}$ . Elastic strains were small than lattice rotations, with radial strains found to be compressive and hoop strains tensile as expected.

Several analyses based on Nye's dislocation tensor were used to estimate the distribution of geometrically necessary dislocations (GNDs) around the indent. The results obtained using different assumed dislocation geometries, optimisation routines, and different contributions from the measured lattice rotation and strain fields are compared. Our favoured approach is to seek a combination of GND types which support the 6 measureable (of a possible 9) gradients of the lattice rotations after correction for the 10 measureable elastic strain gradients, and minimise the total GND line energy using an  $L^1$  optimisation method. A lower bound estimate for the noise on the GND density determination is  $\sim\pm 10^{12} \text{ m}^{-2}$  for a 200 nm step size and near the indent densities as high as  $10^{15} \text{ m}^{-2}$  were measured. For comparison a Hough-based analysis of the EBSD patterns has a much higher noise level of  $\sim\pm 10^{14} \text{ m}^{-2}$  for the GND density.

## Introduction

Indentation has been used for a long time as a convenient means of probing the mechanical properties of materials. The introduction of instrumented indenters has significantly increased the flexibility of indentation testing and interest in testing thin films and small material volumes has generated a large user base for nanoindenters. Indentation testing has been applied to a wide range of materials systems to generate mechanical property data including hardness, elastic modulus, film delamination, residual stresses, and fracture toughness.

One of the fundamental aspects of indentation testing is the well known indentation size effect (ISE). Although hardness values remain constant for large indents made with conical or pyramidal indenters, as the indentation depth is decreased below a micron or so there is a marked increase in the measured hardness. This ISE has been demonstrated in many materials including for example silver [1], tungsten and molybdenum [2], iridium [3] and is not an artefact of sample preparation. Nix and Gao [4] have given a convincing explanation of the effect in terms of geometrically necessary dislocations (GNDs) that are generated as the indent is formed. Some modifications have been made to the original analysis to account for the finite volume around the indent in which the GNDs are accommodated. However, in each case the GNDs are accommodated in smaller volumes of material for shallow indents leading to an increase GND density. Nix and Gao [4] showed that the average GND density near the indenter should be proportional to the reciprocal of the indenter depth. At sufficiently shallow indents the GND density can dominate over the statistically stored dislocations and make a marked contribution to the flow stress and hence hardness. Despite the importance of the ISE and its link to strain gradient plasticity (especially those variants based on GNDs) there have been very few independent measurements of GND density near indentations with which to validate the Nix and Gao theory. Indeed the understanding of flow fields around indentations is generally poor, with simple approximate models such as Johnson's cavity model often used.

Nye [5] gave an elegant geometrical link between lattice curvature and continuous distributions of GNDs described through the dislocation tensor. Nye's analysis was conducted under the assumption that there is no long range elastic strain field (i.e. stress field) present in the crystal. Removal of such an assumption introduces elastic strain gradients (i.e. stress gradients) into the formulation in addition to the lattice rotation gradients used by Nye, as has been discussed in detail by Kroner [6].

Electron back scatter diffraction (EBSD) has been used by several groups to study localised plastic deformation. Early attempts used the contrast reduction and blurring of the EBSD patterns caused by defects within the diffracting volume as a measure of the extent of cold work [7, 8], but with the advent of automated EBSD mapping interest has moved to correlating various measures of the misorientations found within the grains with imposed plastic deformation [9-11]. Adams and co-workers [12, 13] were the first to attempt to use Nye's framework to recover GND densities from electron back scatter diffraction (EBSD) measurements of the spatial variation in crystal orientation. Their studies examined GND accumulation near grain boundaries in deformed Al bi- and poly-crystalline samples. Field *et al* [14] also used the method described by Adams and co-workers to determine the microscale GND distribution in high purity Al single crystals deformed in compression. Pantleon [15] has recently pointed out that earlier analyses [12, 13] used too approximate a treatment for extracting the rotation terms and consequently lost some information that would further constrain the GND solution. Pantleon shows that five terms in Nye's dislocation tensor can be established directly from the EBSD measurements, and that the difference between two other terms can also be calculated and used as a further constraint on the GND solution. Pantleon applies his analysis to GND storage within a cold rolled Al polycrystal and demonstrates an improved lower bound solution is obtained when all six constraints are used.

Wilkinson, Meaden and Dingley [16] have recently developed a new cross-correlation based analysis of EBSD patterns which allows rotations to be measured at much greater sensitivity of  $\sim 0.01^\circ$  compared to  $1^\circ$  to  $0.5^\circ$  with 'conventional' Hough transform based analysis. This development removes much of the cumbersomeness in earlier work by Wilkinson [17, 18] in which a large screen to sample distance was used to achieve the angular resolution. The increased sensitivity gives clear benefits in the recovery of GND density, which has been demonstrated by analysis of plastic deformation at the tip of a fatigue crack tip [19]. Further references concerning the EBSD technique can be found in the following reviews [20, 21].

Here we report high resolution EBSD measurements of lattice curvature near nano-indenters in Fe and determine from them GND distributions.

## Experimental Method

The test sample was a Fe – 0.01wt% C polycrystal obtained from Metal Crystals & Oxides Ltd. (Cambridgeshire, UK) with a grain size of ~ 50  $\mu\text{m}$ . After polishing to 1  $\mu\text{m}$  diamond paste the sample was electropolished in an electrolyte of 10% perchloric acid and 90% acetic acid at 19 volts and ~20°C for 45 seconds. Indents were made with a diamond Berkovich indenter tip using an MTS Nanoindenter XP. The indents were made under constant indentation strain rate of 0.05  $\text{s}^{-1}$ , where the indentation strain rate is defined as indenter tip speed divided by indent depth. The orientation of the indented grain is illustrated by the wireframe inset in fig. 1a, and is described by the following Euler angles  $\phi_1=307^\circ$ ,  $\Phi=32^\circ$ ,  $\phi_2=89^\circ$ .

EBSD measurements were made in a JEOL JSM 6500F FEG SEM operated at 20 keV, and a probe current of 2 nA. A peltier cooled CCD camera (Digiview 12) with 1300 x 1030 pixels and intensities digitised to 12 bit controlled by TSL OIM<sup>1</sup> software was used to capture the EBSD patterns. Measurements were made on the indented surface of the sample from which we obtained maps at a step size of 200 nm around the indents. Patterns were recorded at the full resolution of the camera for subsequent batchwise off-line analysis using CrossCourt 2.0 from BLG Productions Ltd<sup>2</sup>. Full details of the cross correlation analysis of EBSD patterns has been given in [16] including the effects of sub-region size, and noise on the patterns.

The quality of the pattern shift measurements can be assessed using the height of the peak found in the cross correlation function. For a given sub-region the cross correlation peak heights are normalised to bring the peak height for the reference pattern (auto-correlation) to unity. If the pattern quality, that is the Kikuchi band contrast and sharpness, becomes reduced due to the presence of severe plastic deformation, or surface contamination the peak heights are reduced. Shadowing from surface topography also reduces the peak height for those sub-regions of the pattern falling within the shadowed part of the phosphor screen. The geometric mean of normalised peak heights for all sub-regions on a given pattern is calculated and used as a single parameter indicating how well the cross correlation pattern matching has been performed. In the current study patterns giving a mean peak height value below a threshold value of 0.3 were rejected. This generally only happened in regions very close to the indent, where both shadowing and severe plastic deformation are present.

Lattice rotations and elastic strains cause small shifts in the positions of zone axes and other features in the EBSD patterns obtained as the electron beam is scanned over the sample. These small pattern shifts are measured using automated image processing based on two dimensional cross-correlation analysis. The shifts at four or more sub-regions widely dispersed across the EBSD patterns are sufficient to directly calculate eight of the nine degrees of freedom contained in an arbitrary strain and rotation. The remaining degree of freedom is the hydrostatic dilatation of the lattice to which this method is insensitive, though it can be recovered if we, not unreasonably, assume that plane stress conditions are met within the diffraction region close to the sample surface. For the results presented here pattern shifts were measured at 20 sub-regions and least squares methods used to calculate the best fit displacement gradient tensor. The quality of this solution was assessed by calculating the angular difference between the shift expected at each of the sub-regions on the basis of the best fit solution and the actual measured shift. These differences were averaged over all 20 sub-regions to give the mean angular error, which provides a useful means of assessing how good the best fit solution is.

## Analysis for GND Content

The analysis for GND content starts from the simple statement that we require continuity in the displacement field, so that integration of displacement ( $\mathbf{u}$ ) around any closed loop generates zero.

$$\oint_C \mathbf{du} = \oint_C \boldsymbol{\beta} \mathbf{dx} = 0, \quad (1)$$

where  $\boldsymbol{\beta}$  is the displacement gradient (or distortion) tensor, such that  $du_i = \beta_{ij} dx_j$ .

<sup>1</sup> EDAX/TSL, Draper, Utah, USA (www.edax.com)

<sup>2</sup> BLG Productions Ltd, 3 Sydenham Road, Bristol, BS6 5SH, UK (www.blgproductions.co.uk)

The displacement gradient tensor is made up of elastic and plastic parts  $\beta^e$  and  $\beta^p$  respectively. Using Stokes theorem the integration around  $C$  can be replaced by integration over any surface patch  $S$  bounded by  $C$ , so that equation 1 can be rewritten as

$$\iint_S \text{curl}(\beta) \, ds = \iint_S \text{curl}(\beta^e + \beta^p) \, ds = 0 \quad (2)$$

For a given location in the crystal equations 1 and 2 must hold for any closed loop  $C$ , and for any surface patch  $S$ , from which it follows that the elastic and plastic parts of the distortion field must be related by

$$\text{curl}(\beta^e) = -\text{curl}(\beta^p) \quad (3)$$

It is also significant to note that equation 1 is related to the Burger's circuit construction from which the net Burgers vector  $\mathbf{B}$  of dislocation lines piercing the loop  $C$ , is obtained from

$$\mathbf{B} = -\oint_C \beta^p \, dx = -\iint_S \text{curl}(\beta^p) \, ds \quad (4)$$

Remembering that Nye's dislocation tensor  $\alpha$  is defined by

$$\mathbf{B} = \iint_S \alpha \, ds \quad (5)$$

So the dislocation tensor can be found directly in terms of the elastic distortion field through

$$\alpha = \text{curl}(\beta^e) \quad (6)$$

Writing this explicitly in terms of derivatives of the elastic strain and rotation fields gives

$$\alpha = \begin{pmatrix} \frac{\partial w_{12}}{\partial x_3} - \frac{\partial w_{31}}{\partial x_2} & \frac{\partial w_{13}}{\partial x_1} & \frac{\partial w_{21}}{\partial x_1} \\ \frac{\partial w_{32}}{\partial x_2} & \frac{\partial w_{23}}{\partial x_1} - \frac{\partial w_{21}}{\partial x_3} & \frac{\partial w_{21}}{\partial x_2} \\ \frac{\partial w_{32}}{\partial x_3} & \frac{\partial w_{13}}{\partial x_3} & \frac{\partial w_{31}}{\partial x_2} - \frac{\partial w_{32}}{\partial x_1} \end{pmatrix} + \begin{pmatrix} \frac{\partial \varepsilon_{12}}{\partial x_3} - \frac{\partial \varepsilon_{13}}{\partial x_2} & \frac{\partial \varepsilon_{13}}{\partial x_1} & \frac{\partial \varepsilon_{11}}{\partial x_3} - \frac{\partial \varepsilon_{12}}{\partial x_2} \\ \frac{\partial \varepsilon_{22}}{\partial x_2} - \frac{\partial \varepsilon_{23}}{\partial x_3} & \frac{\partial \varepsilon_{23}}{\partial x_1} & \frac{\partial \varepsilon_{21}}{\partial x_2} - \frac{\partial \varepsilon_{22}}{\partial x_1} \\ \frac{\partial \varepsilon_{32}}{\partial x_3} - \frac{\partial \varepsilon_{33}}{\partial x_2} & \frac{\partial \varepsilon_{33}}{\partial x_1} & \frac{\partial \varepsilon_{31}}{\partial x_2} - \frac{\partial \varepsilon_{32}}{\partial x_1} \end{pmatrix} \quad (7)$$

High resolution EBSD measurements allow the rotation and strain field to be mapped over a two dimensional grid on the sample surface, however the variation with depth is not obtained. This means that

terms containing  $\frac{\partial}{\partial x_3}$  are unknown leaving only three of the nine elements of the dislocation tensor fully

determined. However, in many instances that we have looked at experimentally, we find that the rotation gradients are considerably larger than the elastic strain gradients, in which case we can either neglect the elastic strain gradients entirely or include those terms that are available experimentally and put the other terms to zero. In this case five of the nine elements of the dislocation tensor are determined directly, and additionally the difference between two elements (specifically  $\alpha_{11} - \alpha_{22}$ ) can also be found, as pointed out by Pantleon [15]. Pantleon's suggestion [15] that this difference between two elements in the Nye tensor can still be determined when elastic strain gradients are included appears to be in error, since the different symmetric and anti-symmetric nature of the strain and rotation tensors prevent the contributions from both of these sources being cancelled by taking the difference between terms in the Nye tensor. Recent work by Demir *et al* [22] use three dimensional EBSD measurements using serial sectioning in a FIB + SEM instrument to access the gradients in the third dimension. In principal this allows all nine elements in the Nye tensor to be determined under the assumption that elastic strain gradients can be neglected.

The elements in Nye's dislocation tensor are related to the densities  $\rho_s$  of different types of dislocations through

$$\alpha_{ij} = \sum_{s=1}^{s_{\max}} \rho_s b_i^s t_j^s \quad (8)$$

Where  $b^s$  is the burgers vector, and  $t^s$  the unit line direction of the  $s^{\text{th}}$  dislocation type. Nye originally considered a set of nine dislocations with line directions and burgers vectors constrained to be along the cube axes of the crystal, in what Sun *et al* [13] refer to as the *simple cubic (SC) deconstruction*. In this case an unambiguous link between the nine elements of  $\alpha$  and the densities of the different types of dislocations can be established. In our case this does not realistically reflect the crystallographic geometry of possible dislocation types in the BCC Fe crystal, however, such an approach may provide a lower bound estimate of the overall dislocation density. In our analysis for the SC deconstruction we will consider only rotation gradients and set terms that cannot be measured to zero.

To better incorporate the crystallography of the Fe sample we can assume that the deformation is supported by movement and storage of dislocations with  $a/2\langle 111 \rangle$  burgers vector slipping on  $\{110\}$  planes. We further assume that the dislocations are represented by either pure screw, or pure edge types. This results in 16 distinct dislocation types (ignoring positive and negative senses) including 4 screw types (with  $\langle 111 \rangle$  line directions) and 12 edge types (with  $\langle 112 \rangle$  line directions). As with the FCC case, which has been looked at by several other authors [13-15, 22, 23], there is considerably redundancy built into the system, so that there are many ways in which the measured values of  $\alpha_{ij}$  (and  $\alpha_{11} - \alpha_{22}$ ) can be supported by the available dislocations. This forces us to use optimisation routines which find dislocation densities that support the measured values of  $\alpha_{ij}$  and minimise some other related parameter. We write the problem with the dislocation densities represented by the column vector  $\rho$  (16 by 1), and the measured rotation and elastic strain gradients making up elements of Nye's dislocation tensor also as a column vector  $\Lambda$  (6 by 1 for analysis neglecting elastic strains, 3 by 1 when elastic strains are fully incorporated) as

$$\mathbf{A}\rho = \Lambda \quad (9)$$

The  $s^{\text{th}}$  column of  $\mathbf{A}$  contains the various terms in the tensor products of the Burger's vector and line direction of the  $s^{\text{th}}$  dislocation type, as required by equations 8 and 7, and describe how an array of these dislocations would distort the crystal lattice. Two distinct possibilities arise in minimisations schemes that can be used to select a solution for the dislocations densities in equation (9). The mathematically simpler of these is the so called  $L^2$  optimisation scheme which finds the solution giving the minimum sum of squares of the dislocation densities. This approach has been adopted by Field *et al* [14], and the solution for the equations can be written explicitly as

$$\rho = \mathbf{A}^T (\mathbf{A}\mathbf{A}^T)^{-1} \Lambda \quad (10)$$

Arsenlis and Parks [23] have explored these optimisation methods in detail for the FCC case in which 18 possible dislocation types are available. Assuming all nine terms in the Nye tensor are known they note that the null space of  $\mathbf{A}$  gives nine linear combinations of dislocation densities  $\rho_s$  which together generate no contribution to the Nye tensor. Such combinations constitute statistically stored dislocations. In our case this situation is slightly different in that we have 16 dislocation types, but can measure only 6 of nine possible effects on the lattice distortion gradient. The null space of  $\mathbf{A}$  is thus slightly larger, containing 10 combinations of the dislocation types that are either statistically stored or generate no distortion gradient that can be measured by the EBSD mapping on a single plane through the sample. The remaining six linear combinations of the dislocation types generate distortion gradients that are measured. The problem with the  $L^2$  optimisation scheme is that there is no real physical argument leading us to expect a solution which minimises the sum of squares of the dislocation densities. We thus explore this scheme here mainly because others have used it and we wish to compare results with this analysis to those obtained by the  $L^1$  optimisation scheme which we favour.

In the  $L^1$  optimisation we seek a solution to equation 9, that minimises the total dislocation line energy. All our dislocations have the same magnitude Burger's vector, so the only difference in their energies is generated by the ratio of energies for edge and screw dislocations

$$\frac{E_{edge}}{E_{screw}} = \frac{1}{1 - \nu} \quad (11)$$

Other groups have sought to minimise the total dislocation density [12, 13, 22] or equivalently line length. This is very similar to the approach taken here but in effect the ratio of energies of edge and screw dislocations are taken as unity rather than  $\sim 1.5$  which is more typical of a metal ( $\nu=1/3$ ). Various numerical schemes are available for solving this type of problem including the classical simplex algorithm. Here we use the optimisation algorithms implemented in MatLab<sup>3</sup>. Again the solution found represents one of many possible solutions that satisfy the minimisation, and equation 9.

## Results

The crystal orientation and the geometry of the indent with respect to the reference axes used are given in figure 1, along with a typical EBSD pattern.

Figure 2 compares parameters used to assess the quality of data obtained using the conventional Hough transform based analysis of the EBSD patterns with their closest equivalents available from the newer cross-correlation based analysis. The image quality map from OIM and the geometric mean peak height map from CrossCourt indicate where pattern contrast is reduced, and where shadowing arises from the topography of the indenter impression on the scanned surface. The variation at the indent edge is much more abrupt for the OIM image quality map (fig 2a). By comparison the peak height map (fig 2c) shows a smoother transition at the indenter edge but continues to give some variation across the flat surface, with lower values generally recorded within the deformed regions close to the indent. The mean error in interplanar angles from the Hough based analysis (fig 2b) also shows a step change at the edge of the indent with an average value of  $\sim 0.5^\circ$ , (or  $\sim 8 \times 10^{-3}$  rads) obtained outside the indent. The mean angular error in the cross-correlation based shift measurements are  $\sim 100$  times smaller; the average value outside the indent being  $\sim 0.005^\circ$ , or  $9 \times 10^{-5}$  rads. In the region marked A in fig. 1a the peak height is somewhat reduced while the mean angular error is slightly raised compared to other regions around the indent. This small effect is caused by surface topology due a slight pile-up of material in this region. It should be noted that previous analysis of the cross-correlation method indicate that the errors are  $\sim 5$  times larger on some components of the strain and rotation tensors than on those with the smallest measurement errors [19, 24]. Thus although the mean angular error gives an indication of how good the best fit solution is the measurement noise will be greater on some components of strain and rotation than others.

### Rotation Fields

One expects the lower error indicated in the cross correlation based analysis to be linked to less noise and greater detail being visible in the maps of the rotation field. This is indeed the case as is clear in figure 3 which shows the rotation field obtained for the Hough transform based analysis (fig 3 a to c) and the cross correlation based analyses (fig 3 d to f) for the same 500 nm deep indent shown in figures 1 and 2. Data are only shown where the mean error in interplanar angles is  $1^\circ$  or less in the Hough transform based analysis, and where geometric mean of the cross correlation peak heights was found to be 0.3 or greater in the cross correlation based analysis, so that regions near and within the indent where the patterns were of poor quality are excluded. The rotation has been decomposed into 3 components about the orthogonal reference axes (see fig 1) using the assumption of small angles and linear superposition (note most EBSD measurements involve larger angles which requires the more complicated multiplicative decomposition). Near face A we expect the plastic flow away from the indenter face to cause lattice rotations that are predominantly about the  $x_1$  axis (ie the  $w_{23}$  component, (fig 3 c and f), and that is seen to be the case. The other two components,  $w_{31}$  about the  $x_2$  axis (fig 3 b and e), and  $w_{12}$  about the sample surface normal  $x_3$  (fig 3 a and d), are both generally smaller than  $w_{23}$  and vary considerably with position along face A, even changing sign from one end to the other. Compared to near face A, the  $w_{23}$  rotations are smaller and of opposite sign near faces B and C. Along the plane bisecting face A parallel to the  $x_2$  axis the indenter has mirror symmetry, however, this symmetry is not maintained in the distribution of  $w_{23}$  rotations. This loss of the indenter symmetry is even more marked for the  $w_{12}$  and  $w_{31}$  components of rotation, and is presumably due to the specific alignment of the available Burgers vectors and slip planes in the indented crystal. The

<sup>3</sup> MatLab, The Mathworks Inc (www.mathworks.com)

directions of the four possible  $a\langle 111 \rangle/2$  burgers vectors are shown in fig 1, and it is clear that these do not have mirror symmetry through face A.

The rotations components generally take values considerably larger than the mean angular error in pattern shifts obtained with the cross correlation analysis. In contrast, the errors associated with the Hough transform based analysis are of comparable magnitude to the rotation fields being measured, and so although similar variations in rotation are seen compared to the cross correlation based analysis the noise level is significantly higher. Noise on the orientation measurements affects the uncertainty in the misorientation axis and becomes very marked as the misorientation angle becomes comparable and indeed smaller than the orientation sensitivity [25, 26]. Bate *et al* [26] derived the following equation for the uncertainty in the misorientation axis  $\phi$ , in terms of the misorientation angle  $\theta$  and the uncertainty in the misorientation angle  $\delta$

$$\phi = \arctan(\delta/\theta) \quad (12).$$

Maps of this uncertainty in the misorientation axis is shown in figure 4. For the Hough transform generated data (fig 4a) the mean error in the interplanar angles was used as an estimate of  $\delta$ , and given the small size of the misorientations present in the data very large uncertainty is generated in the misorientation axis information. It is only in the most highly misoriented regions that there is any real confidence in the misorientation axis. In contrast the cross correlation generated data (fig 4b) retain higher confidence in the misorientation axis across the whole field because of the much smaller error in the misorientation angle  $\delta$  (taken to be the mean angular error in the pattern shifts).

### Elastic Strain Fields

The cross correlation analysis has sufficient sensitivity for the variation in elastic strains to be mapped in addition to the lattice rotation. Maps of selected components of the elastic strain tensor for this indent are given in figure 5, again data is only shown if the geometric mean of cross correlation peak heights is 0.3 or above. The strains are generally smaller than for the rotations and so these maps appear a little noisier than those in figure 3, however, systematic elastic strain variations are clearly resolved by the method. The elastic strains are referred to polar coordinates with the origin marked on the figures at the centre of the indent. The radial strains are seen to be generally compressive, while the hoop strains are generally tensile which is in line with expectations. The triangular pyramid shape of the indenter imparts some angular variation of these strains not captured by axisymmetric models such as Johnson cavity model. These angular variations of strains is further promoted by the crystallographic anisotropy of plastic slip relieving stresses in some directions more effectively than others. The in plane  $\epsilon_{r\theta}$  shear strains not accounted for in axisymmetric models are also present at significant levels, though are limited to small regions close to the indent and fall off quickly to small values at larger radii. The other elastic strain components, that is normal, and shear strains containing out of plane displacements are significantly smaller and are not shown here.

### GND Content

Various routes for constructing maps of the GNDs density distributions near the indent using the Nye/Kroner analysis have been explored. Summary results showing the total GND density fields are compared in figure 6. The maps in figures 6a and 6b were constructed from Hough based analysis of the lattice rotation field. It is difficult to discern much obvious structure to the storage of GND in the plastic zone near the indent. A simple lower bound estimate of the expected noise on these GND measurements, can be made from the uncertainty in the orientation measurements  $\delta = 8 \times 10^{-3}$  rads and the step size used in the EBSD map  $\lambda$  of 200 nm using the simple expression

$$\Delta\rho = \frac{\delta}{b\lambda} \quad (13)$$

Which gives a large uncertainty in the GND density of  $\sim 2 \times 10^{14} \text{ m}^{-2}$ , which masks the underlying distribution. GND distributions generated from the cross correlation based analysis of the EBSD patterns (figure 6 c to h) exhibit a reduced noise level, estimated to be  $\sim 2 \times 10^{12} \text{ m}^{-2}$  and allow the plastic zone to be revealed.

This simple estimate ignores the influence of misorientation axis and the manner in which errors are compounded by the addition of densities on many slip systems. Analysis of EBSD maps on well annealed samples away from any indent indicate a noise level of  $\sim 10^{13} \text{ m}^{-2}$  for the total GND content under the BCC deconstruction. Comparing figures 6 (c) and (d) shows that the simple SC deconstruction generates a significantly lower estimate of the total GND density than the BCC deconstruction. Curvatures are less efficiently accommodated in the BCC deconstruction because the true crystallography leads to a system of dislocations with Burgers vectors (and indeed line directions) that are not mutually orthogonal. The two optimisation methods are compared in figures 6 (d) and (e), where it is seen that in this instance the  $L^2$  scheme which has less physical basis leads to a very similar pattern for the GND distribution and generates densities that are marginally higher than for the  $L^1$  scheme which we prefer. As expected from the smaller magnitudes of the elastic strains, inclusion of elastic strain gradients as corrections to the curvatures calculated from the rotation field only leads to small changes in the estimate of the GND density. This can be seen by comparing figures 6 (d) and (f) though here not all terms required to fully correct for the strain gradients are available. If we limit the analysis to just three terms in the Nye tensor then it is again seen that inclusion of the elastic strain gradient has only a small effect (cf figures 6 g and h). A much more significant effect on the GND estimate is that using only three terms in the Nye tensor leads to significantly lower values for the GND density (cf figures 6 f and g, and figures 6 d and h).

Our preferred method is to use the six available derivatives of the lattice rotations corrected for the available elastic strain gradients within an  $L^1$  optimisation to minimise the total line energy (ie fig 6f). We also note that having some of the elastic strain fields measured allows us to assess whether or not the neglect of some elastic strain gradients is likely to lead to large errors in determining the GND content. Figure 7 shows the distribution of each of the 16 individual GND types making up the BCC deconstruction. It should be noted that there is a non-uniqueness issue within this analysis so that this is one possible solution that satisfies the measured lattice curvatures and minimises the total dislocation line energy. The fact that regions of higher density for particular GND types are spatially correlated gives some support to the idea that this particular solution is a reasonable one. Furthermore the dislocation densities appear to be of reasonable magnitudes. In figure 7 negative dislocation densities simply mean that the sense of the dislocation is the opposite of that indicated by the 'clockface' found toward the top left of each map. This 'clockface' indicates the projection of the Burger's vector onto the sample surface plane. A Burgers vector fully in the surface plane reaches to the edge of the circle while in other cases the component in the surface plane determines the length, while colour (on-line version) is used to indicate whether the out of plane component is into (red) or out-of (green) the sample surface. A similar approach is taken for the line direction shown black if out-of the sample and blue if into the sample.

It is noticeable that the lower line energy of the screw dislocations generally leads to them being present in greater densities (fig 7 a to d) than the edge types (fig 7 e to p). In many cases the regions of high density for a particular dislocation type are in bands that radiate out from the indent. In some instances (eg fig 7g) there are several parallel bands extending out from different parts of the indent. Figure 7 suggests that some dislocation types are considerably less populated than others, notably the edge dislocation in fig 7k and fig 7m, and of the screw dislocations those in fig 7d. There are several possibly reasons for the lower populations of some types of GND in the optimal solution: (i) these dislocations are simply not present, (ii) the geometry of the dislocations leads to curvatures that are not readily detected, or, (iii) these dislocations may be present but are not reflected by the optimisation to minimise line energy. Examining the magnitudes of terms in the columns of matrix **A** helps to rule out possibility (ii) as we find that in this particular crystal orientation all the dislocation types should generate measureable curvatures of similar size. Indeed the norms of columns making up **A** have an average of 0.19 and a standard deviation of 0.04.

## Discussion

The cross correlation analysis of the EBSD patterns clearly achieves higher sensitivity than the more standard Hough transform based analysis. Visual comparison of the lattice rotation fields obtained from the Hough-based and cross correlation-based analysis (fig 3) tend to suggest that the Hough-based analysis is able to pick up the underlying trends despite the significantly greater noise level. However, the uncertainty in the rotation axis (fig 4) is marked and produces a large uncertainty in determining any information concerning the Burgers vector and line direction of the dislocations giving rise to the rotation. The need for lattice rotation (and elastic strain) gradients in the analysis for GND content exacerbates the noise problem since (numerical) differentiation tends to always leads to increased noise. With the step size used here a simple analysis leads to a lower bound estimate of the noise on the GND density of  $\sim 10^{14} \text{ m}^{-2}$  for the Hough-based analysis. This is already well into the densities expected for quite extensively cold worked

1  
2  
3 metals so that only the very extreme GND densities can be reliably measured. At first glance equation 13  
4 suggests that increasing the step size for the EBSD map would lead to increased sensitivity in the GND  
5 density measurement, however, increasing the step size also increases the likelihood of there being  
6 combinations of dislocations between the measurement points that make no (or reduced) contribution to  
7 the lattice curvature. In other words keeping the step size small has the attraction that a larger fraction of  
8 the dislocation content can be thought of as GNDs which we can detect, rather than statistically stored  
9 dislocations which are missed in the analysis. Attempts to reduce noise by using more than two  
10 measurement points to define the orientation gradient would, for a given step size, also increase the  
11 effective length scale over which the GND content was assessed and may omit real features present at  
12 shorter lengths. Such step size dependence of more empirical measures of deformation from EBSD  
13 determined misorientation maps have been explored by LeHockey [11] and Kamaya et al [9]. In  
14 comparison at  $\sim 10^{12} \text{ m}^{-2}$  the lower bound estimate of the noise level on GND content derived from the  
15 cross correlation analysis of EBSD patterns is such that dislocation structures in deformed or even  
16 annealed metals can be assessed, as indeed can strains and defect content in semiconductor materials  
17 and structures.

18 The range of applications of this cross correlation based analysis of EBSD patterns is large and so it is  
19 important to generate parameters that allow the quality of patterns and data extracted from them to be  
20 assessed in an automated and quantitative way so that the rapidly growing size and number of linescans  
21 and maps that are generated can be used with confidence. Two such parameters, namely the geometric  
22 mean of the normalised cross correlation peak heights and the mean angular error in the measured pattern  
23 shifts usefully perform this function. Figure 2 demonstrates that they can both be used to distinguish  
24 between regions in a map where the data is sound and where it is of poorer quality, in this case inside the  
25 indent.

26 Systematically mapping dislocation densities in the range  $10^{12}$  to  $10^{16} \text{ m}^{-2}$  over areas of the size studied  
27 here or even larger, would be too labour intensive to undertake using TEM and would require painstaking  
28 or possibly prohibitive sample preparation. Conventional x-ray and neutron diffraction methods can probe  
29 dislocation densities in this range using peak broadening analysis; however, this provides only volume  
30 averaged information. The EBSD method provides a means of probing dislocation arrangements at the  
31 mesoscopic and microscopic length scales and so is an important bridge between analysis of individual  
32 defects in the TEM and volume averaged densities available through x-ray and neutron probes. It is of  
33 course at these mesoscopic length scales that many important phenomena occur during plastic  
34 deformation as a result of complex interactions between dislocations and microstructural features. Some  
35 synchrotron based x-ray diffraction techniques [27-29] do provide information that is more directly  
36 comparable to that obtained with EBSD. These approaches have the advantage that the full three  
37 dimensional nature of the problem can be addressed, but have the disadvantages of lower spatial  
38 resolution and the inconvenience and cost associated with large centralised facilities with limited access.  
39 Vaudin *et al* [30] have recently used EBSD patterns and CrossCourt software to measure deformation  
40 approaching a wedge indent in Si. To ease direct comparison with micro-Raman measurements from the  
41 same indents they present the EBSD results for the variation of in plane biaxial stress, which is shown to  
42 follow a  $1/r^2$  dependence, with  $r$  being the distance from the central line of the indent. This is the variation  
43 expected from a simple comparison with the elastic strains and stresses close to an expanding cylindrical  
44 cavity. The EBSD results also agree extremely well with micro-Raman measurements when suitable  
45 exciting illumination is selected to minimise the penetration into the sample depth. In our case the  
46 analogous elastic analysis is of a spherical cavity a leads to a  $1/r^3$  variation of elastic strains. However,  
47 there is markedly more plasticity near the indent in Fe compared to Si and so the resulting elastic strains  
48 are smaller and do not show as simple a trend.

49 Kysar *et al* [31] have used Hough-based EBSD to examine sub-surface deformation in cross sections  
50 through relatively deep (several hundred microns) wedge indents in Cu and Al single crystals. Lattice  
51 rotations below these indents were significantly larger, at up to  $20^\circ$ , than those seen here at the free  
52 surface for much smaller indents. Plane strain conditions were assumed in a GND analysis of the lattice  
53 curvatures leading to a reduced set of dislocation types the densities of which are found using the less  
54 physical  $L^2$  minimisation scheme. Although the symmetry of the crystals and indenter do imply plane strain  
55 conditions at a macro-scale at the mesoscopic scale probed by EBSD this may not be the case. It may be  
56 of interest to use a more general analysis such as that presented here and use this to examine the extent  
57 to which constraints on the deformation expected from a macroscopic viewpoint are in fact followed at the  
58 more local level within the dislocation sub-structure.

59 Hough-based EBSD studies of sub-surface deformation for indents in Cu have also been made by Demir *et al* [22].  
60 They studied conical indents at depths from 450 nm to 1230 nm, using repeated sectioning in a FIB-SEM  
instrument to probe the 3 dimensional structure. Again large rotations are seen below the indents making  
the Hough-based analysis possible, though they note a noise level of  $\sim 10^{14} \text{ m}^{-2}$  on the derived GND

1  
2  
3 densities in accord with our estimation here. Rester *et al* [32] have also used Hough-based EBSD to map  
4 orientation changes below cube-corner indents in Cu and note that the self-similar pattern in the  
5 misorientations breaks down for very shallow indents below ~300 Nm deep, and indeed for very large  
6 indents to depths greater than ~30  $\mu\text{m}$ .

7 The Nix-Gao theory [4] for the ISE assumes that the GNDs are stored in a hemispherical region below the  
8 indenter contact in a uniform distribution. Furthermore for convenience the GNDs are considered to be  
9 arranged as prismatic loops with Burgers vectors perpendicular to the surface which are rather efficient at  
10 accommodating permanent impression made by the indenter. For a Berkovich indent of 500 nm depth in  
11 Fe the Nix-Gao model gives a GND density of  $\sim 1.5 \times 10^{15} \text{ m}^{-2}$  and densities close to this were determined  
12 from the EBSD measurements, and may be even higher below the indented surface. In the experiment it is  
13 clear that the GNDs are far from uniformly distributed despite the availability of many slip systems in BCC  
14 structure. In some place the high GND densities extend a considerable distance beyond the indent  
15 impression, and the predominant burgers vector varies around the indent in a complex way. The detailed  
16 interaction of the triangular indenter and motion and accumulation of dislocations in the crystal is not  
17 captured by the Nix-Gao model which necessarily simplifies the geometry to generate a tractable problem.  
18 Crystal plasticity finite element analysis by Liang *et al* [33] has been used to simulate the deformation  
19 around the indent studied here. The ISE is captured in the simulation which includes hardening from GNDs  
20 which are allowed to evolve (increase and decrease) in response to changes in the plastic strain gradient.  
21 Lattice rotations are predicted by the model and are in qualitative agreement with experiment. The  
22 magnitudes of the rotations are slightly over predicted but this may be due to omission of the unloading  
23 phase from the simulations.  
24  
25

## 26 Conclusions

27  
28 We have used a cross correlation based analysis of EBSD patterns to map the variation of the elastic strain  
29 tensor (and hence stress tensor) and small lattice rotations in the vicinity of a 500 nm deep Berkovich  
30 indent in Fe. Two measures of the data quality have been developed which successfully identify regions  
31 where shadowing and severely blurred patterns prevent sensible analysis from being undertaken. These  
32 are the geometric mean of the normalised cross correlation peak heights and the mean angular error in the  
33 measured pattern shifts. Lattice rotations are significantly larger than elastic strains. The radial elastic  
34 strains are generally compressive and the hoop strains tensile as expected, though the variation is strongly  
35 influenced by the anisotropy in the plastic flow. Direct comparison of maps from the cross correlation  
36 based analysis with those from the conventional Hough-based analysis clearly demonstrate the improved  
37 sensitivity of the cross correlation technique.

38 Analyses for the GND content was undertaken assuming dislocation types representative of both simple  
39 cubic and body centred cubic crystals and using as inputs various components of the gradients of the  
40 lattice rotations and elastic strains. Our favoured approach is to seek a combination of GND types which  
41 support the 6 measureable (of a possible 9) gradients of the lattice rotations after correction for the 10  
42 measureable elastic strain gradients, and minimise the total GND line energy using an  $L^1$  optimisation  
43 method. The corrections for elastic strain gradients neglect 3 terms that cannot be measured as gradients  
44 along the surface normal are not accessible. The solution thus forms a lower bound estimate of the GND  
45 density. The  $\pm 10^{-4}$  sensitivity of the cross correlation analysis corresponds to a lower bound estimate of  
46  $\pm 10^{12} \text{ m}^{-2}$  for the noise on the GND density for a 200 nm step size. GND densities as high as  $10^{15} \text{ m}^{-2}$  were  
47 found near the indent. The lower line energy of the screw dislocations makes them more favoured in the  
48 solution, and regions where specific dislocation types are located are observed in the solution.  
49  
50

## 51 Acknowledgements

52 Thanks to (i) Dr Mark Vaudin (NIST, Gaithersburg) for discussion of EBSD results on indents in Si prior to  
53 publication and initial MatLab script for plotting maps from CrossCourt output, (ii) Dr Graham Meaden (BLG  
54 Productions Ltd) and Prof David Dingley (University of Bristol) for continuing discussion of all aspects of  
55 EBSD (iii) Prof Fionn Dunne (University of Oxford) and Dr Hong Liang (University of Oxford) for insightful  
56 discussions on their crystal plasticity simulations of indentation, and (iv) Ben Britton (University of Oxford)  
57 for discussions on GND analysis and extensive input into Matlab coding.  
58  
59  
60

## Figure Captions

Figure 1: (a) secondary electron image of 500 nm deep Berkovich indent in Fe with isets showing the crystal orientation and the trace of  $\langle 111 \rangle$  slip directions in the surface plane. (b) An EBSD pattern from the crystal with sub-regions used for cross correlation analysis marked.

Figure 2: maps showing EBSD data quality. (a) image quality index based on height of peaks found in Hough transform, (b) mean error in interplanar angles from Hough based analysis (in degrees), (c) geometric mean of normalised cross correlation peak heights, and (d) mean angular error in pattern shifts determined in cross correlation based analysis (in degrees).

Figure 3: lattice rotation fields measured by Hough based analysis (a to c) and cross correlation based analysis (d to f). Rotation angles are in radians.

Figure 4: Estimated error in alignment of misorientation axis (in degrees) for (a) Hough based analysis and (b) cross correlation based analysis.

Figure 5: Selected elastic strain components given in cylindrical polar co-ordinates referred to an origin marked at centre of the indent. Other components are also determined but are markedly smaller.

Figure 6: Estimates of GND density distribution near indent. [Colourscale shows  $\log(\rho)$  with  $\rho$  in lines/m<sup>2</sup>.]

- Hough based rotation fields, strains not measured, SC deconstruction of 6 terms in  $\alpha$ .
- Hough based rotation fields, strains not measured, BCC deconstruction of 6 terms in  $\alpha$ .
- cross correlation based rotation fields, strains neglected, SC deconstruction of 6 terms in  $\alpha$ .
- cross correlation based rotation fields, strains neglected, BCC deconstruction of 6 terms in  $\alpha$ ,  $L^1$  optimisation.
- cross correlation based rotation fields, strains neglected, BCC deconstruction of 6 terms in  $\alpha$ ,  $L^2$  optimisation.
- cross correlation based rotation fields, corrected for measured elastic strain gradients, BCC deconstruction of 6 terms in  $\alpha$ ,  $L^1$  optimisation.
- cross correlation based rotation and strain fields, BCC deconstruction of 3 terms in  $\alpha$ ,  $L^2$  optimisation.
- cross correlation based rotation fields, BCC deconstruction of 3 terms in  $\alpha$ ,  $L^2$  optimisation.

Figure 7: One possible solution for densities of the 16 different GND types assumed in the BCC deconstruction of cross correlation based rotation fields, corrected for measured elastic strain gradients to give 6 terms in  $\alpha$ .  $L^1$  optimisation to give a minimal line energy solution was used. The 'clockfaces' show the projection of the Burger's vector and line directions onto the sample surface plane. Burgers vectors are red or green to indicate a component along  $x_3$  that is into or out-of the surface plane. Line directions are shown black if out-of the sample and blue if into the sample. (a) to (d) show the four screw dislocations while (e) to (p) the 12 edge types.

## References

- [1] Q. Ma and D. R. Clarke, *J. Mater. Res.* 10 (1995)
- [2] N. A. Stelmashenko, M. G. Walls, L. M. Brown and Y. V. Milman, *Acta Metall. Mater.* 41 (1993)
- [3] J. G. Swadener, E. P. George and G. M. Pharr, *J. Mech. Phys. Solids* 50 (2002)
- [4] W. D. Nix and H. J. Gao, *J. Mech. Phys. Solids* 46 (1998)
- [5] J. F. Nye, *Acta Metallurgica* 1 (1953)
- [6] E. Kroner, *Continuum theory of dislocations and self stresses*, Springer-Verlag, Berlin, 1958
- [7] A. J. Wilkinson and D. J. Dingley, *Acta Metall. Mater.* 40 (1992)
- [8] P. N. Quested, P. J. Henderson and M. McLean, *Acta Metallurgica* 36 (1988)
- [9] M. Kamaya, A. J. Wilkinson and J. M. Titchmarsh, *Nucl. Eng. Des.* 235 (2005)
- [10] M. Kamaya, A. J. Wilkinson and J. M. Titchmarsh, *Acta Mater.* 54 (2006)
- [11] E. M. Lehockey, Y. Lin and O. E. Lepik, *Electron Backscatter Diffraction in Materials Science* (2000)
- [12] B. S. El-Dasher, B. L. Adams and A. D. Rollett, *Scr. Mater.* 48 (2003)
- [13] S. Sun, B. L. Adams and W. E. King, *Philos. Mag. A-Phys. Condens. Matter Struct. Defect Mech. Prop.* 80 (2000)
- [14] D. P. Field, P. B. Trivedi, S. I. Wright and M. Kumar, *Ultramicroscopy* 103 (2005) p.33.
- [15] W. Pantleon, *Scr. Mater.* 58 (2008)
- [16] A. J. Wilkinson, G. Meaden and D. J. Dingley, *Ultramicroscopy* 106 (2006)
- [17] A. J. Wilkinson, *J. Electron Microsc.* 49 (2000)
- [18] A. J. Wilkinson, *Ultramicroscopy* 62 (1996)
- [19] A. J. Wilkinson, G. Meaden and D. J. Dingley, *Mater. Sci. Technol.* 22 (2006)
- [20] A. J. Wilkinson and P. B. Hirsch, *Micron* 28 (1997)
- [21] F. J. Humphreys, *J. Mater. Sci.* 36 (2001)
- [22] E. Demir, D. Raabe, N. Zaafarani and S. Zaefferer, *Acta Mater.* 57 (2009) p.559.
- [23] A. Arsenlis and D. M. Parks, *Acta Mater.* 47 (1999)
- [24] S. Villert, C. Maurice, C. Wyon and R. Fortunier, *J. Microsc.-Oxf.* 233 (2009)
- [25] A. J. Wilkinson, *Scr. Mater.* 44 (2001)
- [26] P. S. Bate, R. D. Knutsen, I. Brough and F. J. Humphreys, *J. Microsc.-Oxf.* 220 (2005)
- [27] B. Jakobsen, H. F. Poulsen, U. Lienert and W. Pantleon, *Acta Mater.* 55 (2007)
- [28] W. Yang, B. C. Larson, J. Z. Tischler, G. E. Ice, J. D. Budai and W. Liu, *Micron* 35 (2003) p.431.
- [29] G. Feng, A. S. Budiman, W. D. Nix, N. Tamura and J. R. Patel, *J. Appl. Phys.* 104 (2008)
- [30] M. D. Vaudin, Y. B. Gerbig, S. J. Stranick and R. F. Cook, *Appl. Phys. Lett.* 93 (2008) p.193116.
- [31] J. W. Kysar, Y. X. Gan, T. L. Morse, X. Chen and M. E. Jones, *J. Mech. Phys. Solids* 55 (2007)
- [32] M. Rester, C. Motz and R. Pippan, *Scr. Mater.* 59 (2008)
- [33] H. Liang, F. P. E. Dunne and A. J. Wilkinson, *International Conference on Heterogeneous Material Mechanics (ICHMM)* (2008)

1  
2  
3  
4  
5  
6  
7  
8  
9  
10  
11  
12  
13  
14  
15  
16  
17  
18  
19  
20  
21  
22  
23  
24  
25  
26  
27  
28  
29  
30  
31  
32  
33  
34  
35  
36  
37  
38  
39  
40  
41  
42  
43  
44  
45  
46  
47  
48  
49

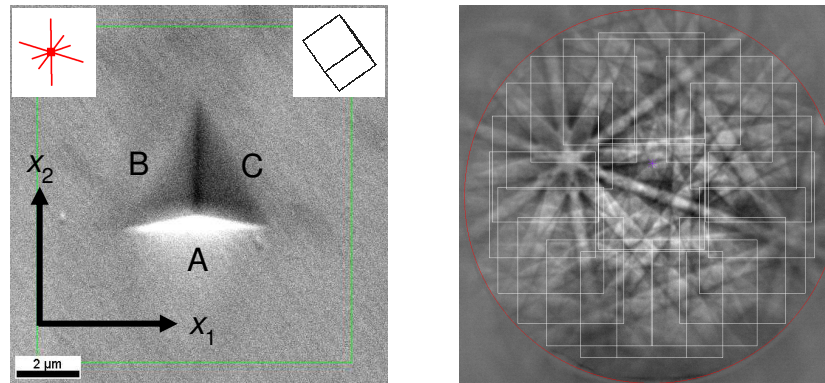


Figure 1

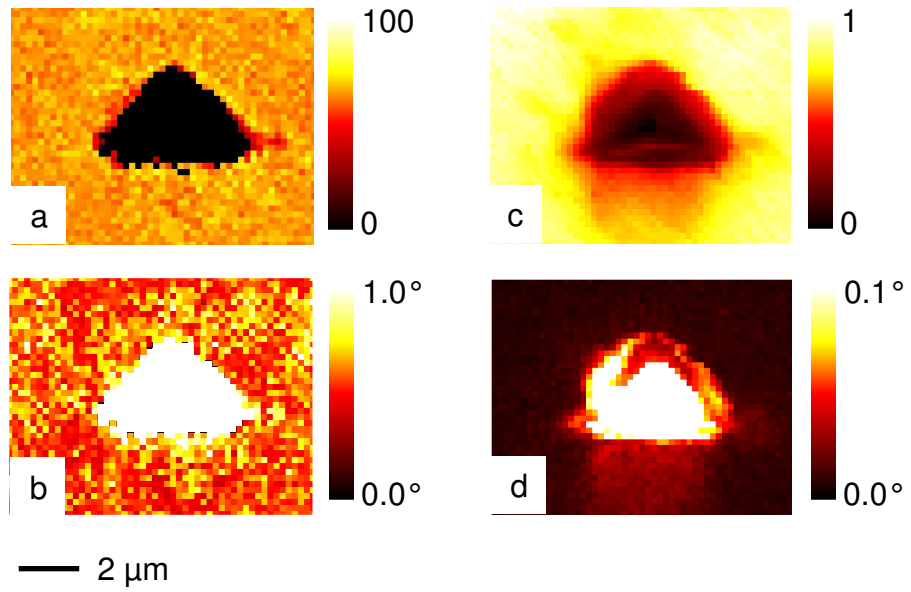


Figure 2

1  
2  
3  
4  
5  
6  
7  
8  
9  
10  
11  
12  
13  
14  
15  
16  
17  
18  
19  
20  
21  
22  
23  
24  
25  
26  
27  
28  
29  
30  
31  
32  
33  
34  
35  
36  
37  
38  
39  
40  
41  
42  
43  
44  
45  
46  
47  
48  
49

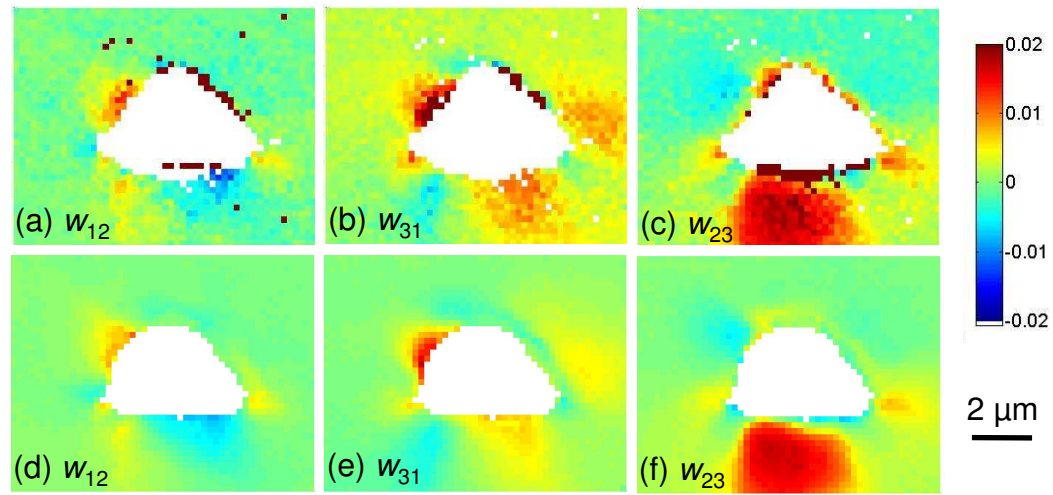


Figure 3

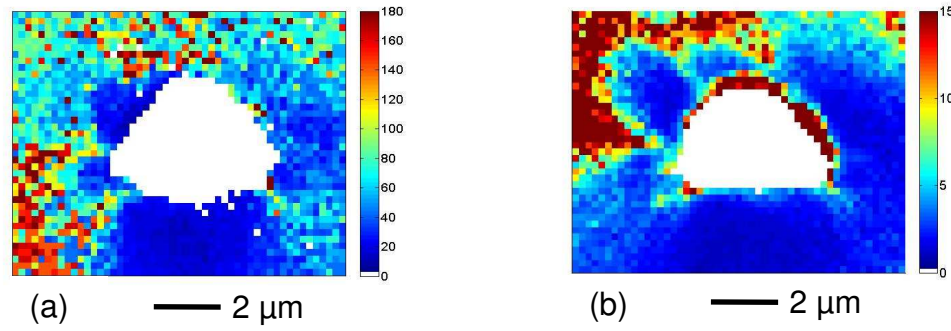


Figure 4

1  
2  
3  
4  
5  
6  
7  
8  
9  
10  
11  
12  
13  
14  
15  
16  
17  
18  
19  
20  
21  
22  
23  
24  
25  
26  
27  
28  
29  
30  
31  
32  
33  
34  
35  
36  
37  
38  
39  
40  
41  
42  
43  
44  
45  
46  
47  
48  
49

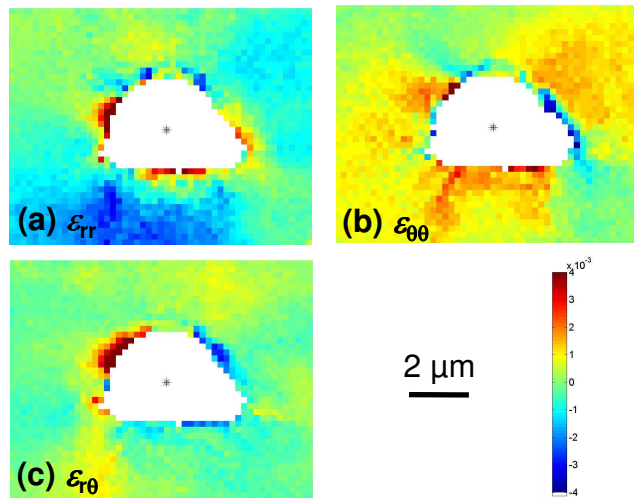


Figure 5

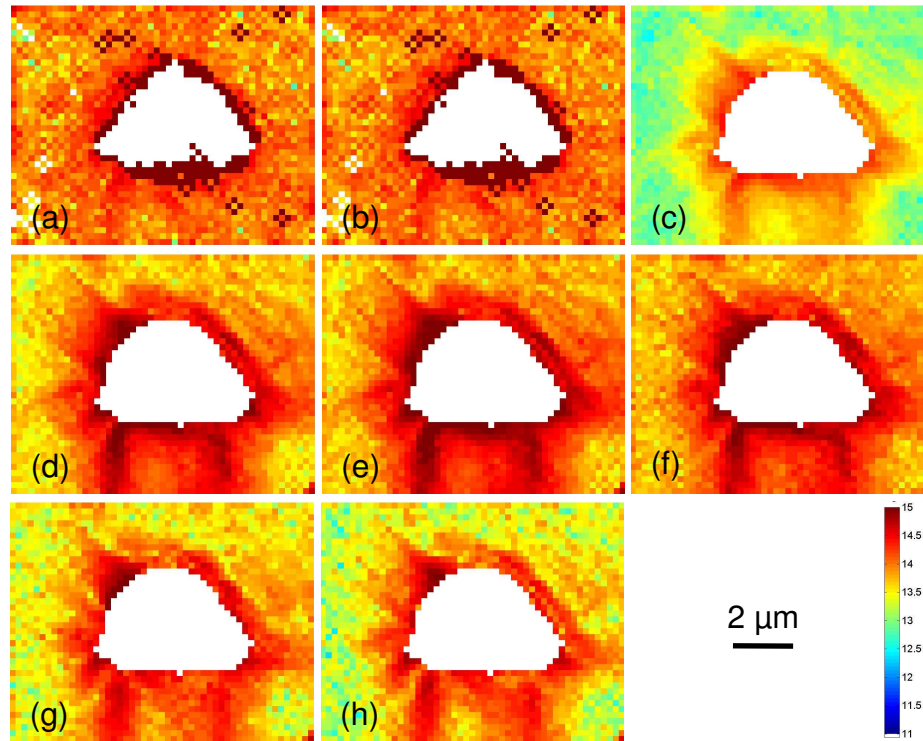


Figure 6

1  
2  
3  
4  
5  
6  
7  
8  
9  
10  
11  
12  
13  
14  
15  
16  
17  
18  
19  
20  
21  
22  
23  
24  
25  
26  
27  
28  
29  
30  
31  
32  
33  
34  
35  
36  
37  
38  
39  
40  
41  
42  
43  
44  
45  
46  
47  
48  
49

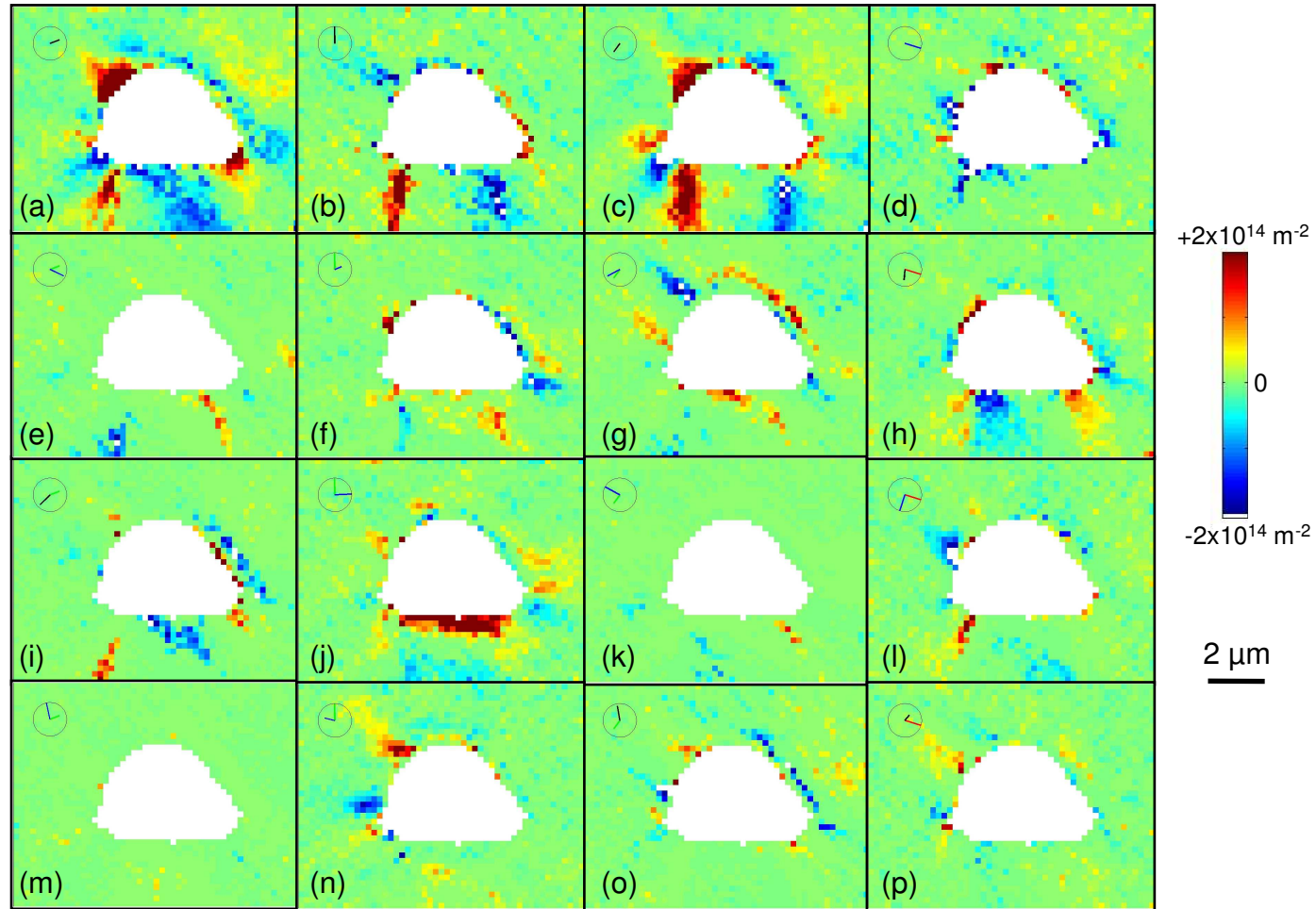


Figure 7